

Strong magnetoelastic coupling in MnCoSi compounds studied in pulsed magnetic fields

Zhang, Fengqi; Bykov, Eduard; Gottschall, Tino; Van Dijk, Niels; Brück, Ekkes

DOI

[10.1103/PhysRevB.107.214431](https://doi.org/10.1103/PhysRevB.107.214431)

Publication date

2023

Document Version

Final published version

Published in

Physical Review B

Citation (APA)

Zhang, F., Bykov, E., Gottschall, T., Van Dijk, N., & Brück, E. (2023). Strong magnetoelastic coupling in MnCoSi compounds studied in pulsed magnetic fields. *Physical Review B*, 107(21), Article 214431. <https://doi.org/10.1103/PhysRevB.107.214431>

Important note

To cite this publication, please use the final published version (if applicable).
Please check the document version above.

Copyright

Other than for strictly personal use, it is not permitted to download, forward or distribute the text or part of it, without the consent of the author(s) and/or copyright holder(s), unless the work is under an open content license such as Creative Commons.

Takedown policy

Please contact us and provide details if you believe this document breaches copyrights.
We will remove access to the work immediately and investigate your claim.

Strong magnetoelastic coupling in MnCoSi compounds studied in pulsed magnetic fields

Fengqi Zhang^{1,*}, Eduard Bykov^{2,3}, Tino Gottschall², Niels van Dijk¹, and Ekkes Brück¹

¹*Fundamental Aspects of Materials and Energy (FAME), Faculty of Applied Sciences, Delft University of Technology, Mekelweg 15, 2629JB Delft, The Netherlands*

²*Dresden High Magnetic Field Laboratory (HLD-EMFL), Helmholtz-Zentrum Dresden-Rossendorf, 01328 Dresden, Germany*

³*Institute of Solid State and Materials Physics, Technische Universität Dresden, 01062 Dresden, Germany*



(Received 25 January 2023; revised 19 April 2023; accepted 13 June 2023; published 21 June 2023)

The orthorhombic MnCoSi compounds have been found to present a large magnetoelastic coupling, which is regarded as the source for the magnetocaloric effect (MCE) and the magnetostrictive effect. As a result, these compounds are potential materials for caloric applications such as solid-state refrigeration. In the present study, we offer fundamental insights in the magnetoelastic coupling in these compounds based on their structural, metamagnetic, and MCE behavior. The directly measured adiabatic temperature change (ΔT_{ad}) in different initial temperatures (down to 18 K) and pulsed magnetic fields (up to 40 T) presents a moderate MCE performance (the maximum $\Delta T_{\text{ad}} = -3.1$ K for a field change of 13 T), which results from the metamagnetic behavior of these compounds. Furthermore, the magnetization measurements in pulsed (and static) magnetic fields indicate that the magnetoelastic coupling is significantly enhanced for increasing fields resulting in an improved saturation magnetization. The metamagnetic transition is continuously pushed to lower temperatures in higher fields. The phase diagram constructed from the experimental transition temperatures T_i and the critical magnetic fields $\mu_0 H_{\text{cr}}$ indicate that the transition is terminated below 18 K and that ferromagnetism is stabilized for fields above 22.3 T. Our results provide unique insights into the strong magnetoelastic coupling under high pulsed magnetic fields, providing guidelines for the design of giant magnetocaloric materials for future caloric applications.

DOI: [10.1103/PhysRevB.107.214431](https://doi.org/10.1103/PhysRevB.107.214431)

I. INTRODUCTION

As a result of the magnetic exchange coupling and the spin-orbit interaction, a magnetoelastic coupling between the magnetic order parameter in the magnetically ordered state and elastic atomic displacements of the lattice can be observed [1]. A strong magnetoelastic coupling is associated with the MCE in metallic ferromagnets [2,3] and the magnetoelectric effect in perovskite materials [4,5]. Magnetocaloric materials (MCMs) that show a MCE with a large magnetoelastic coupling include (Mn, Fe)₂(P, X)-based (X = As, Ge, Si) [2,6], La(Fe, Si)₁₃-based [7], FeRh-based [8], Eu₂In [9], and MnCoSi [10] compounds. These MCMs enable promising application scenarios such as solid-state magnetic refrigeration [11], magnetic heat pumps [12], and thermomagnetic generators to convert low-temperature waste heat into electricity [13–15]. For magnetic systems, it is known that the energy operator Hamiltonian \mathcal{H} can be expressed [1] as $\mathcal{H} = \mathcal{H}_m + \mathcal{H}_e + \mathcal{H}_{me} + \mathcal{H}_a$, where \mathcal{H}_m is the magnetic energy, \mathcal{H}_e the elastic energy, \mathcal{H}_{me} the magnetoelastic coupling, and \mathcal{H}_a the anisotropy energy. The energy of the system is minimized by aligning the magnetization in the lowest-energy direction and with a subtle elastic lattice distortion resulting from the coupling of the magnetic order and the elastic energy via the magnetoelastic coupling. The simplest manifestation of the magnetoelastic coupling is the magnetostriction, where the lattice is elastically deformed in the presence of externally applied magnetic fields [1,16,17].

As an intriguing class of magnetoelastic MCMs [10], the MnCoSi compounds with an orthorhombic NiTiSi type crystal structure have been widely studied [18–20]. It was observed that these compounds hold the largest magnetoelastic coupling in metallic magnets [21], which is responsible for the spontaneous transition from the low-temperature noncollinear antiferromagnetic (AFM) to the high-temperature ferromagnetic (FM) state. This strong coupling is mainly tailored by the metastable nearest Mn-Mn distance [21,22]. Although the physical properties below 9 T have been investigated for the MnCoSi family [22], the metamagnetic properties at higher magnetic fields (>10 T) are still lacking. Nondestructive pulsed field facilities provide the possibility to significantly extend the magnetic field range (up to 50 T and beyond) by establishing the phase diagram of T_i and $\mu_0 H_{\text{cr}}$ and probe the magnetic properties of the AFM/FM state. As the timescale of the pulsed magnetic fields (10–100 ms) matches the targeted operation frequency of magnetic refrigerators (10–100 Hz) [23,24], pulse field measurements can directly characterize the adiabatic temperature change (ΔT_{ad}) to evaluate the MCE under adiabatic conditions. The method has been applied for several MCMs such as Ho₂Fe₁₇ [25], rare earth based Laves phase compounds [26–28], Gd [29,30], MnFe₄Si₃ [31], FeRh [32], La(Fe, Si)₁₃ [33], and NiMn-based Heusler compounds [23,24,34–36]. These previous studies enable the exploration of MnCoSi materials in pulsed magnetic fields.

Consequently, a Mn_{1.02}Co_{0.98}Si compound has been produced and its structural, magnetization, and MCE properties were studied under static (up to 14 T) and pulsed (up to 40 T) magnetic fields. The *in situ* pulse-field measurements

*F.Zhang-7@tudelft.nl

enable the simultaneous determination of the magnetization and the adiabatic temperature change ΔT_{ad} around the metamagnetic transition for different temperatures, magnetic fields, and timescales (pulse duration). The results demonstrate that the metamagnetic transition in MnCoSi MCMs is connected with the strong magnetoelastic coupling and provides insights into the strong magnetoelastic coupling in high pulsed magnetic fields.

II. METHODS AND EXPERIMENTAL PROCEDURE

High-purity (99.9%) raw materials were used to prepare polycrystalline samples with a nominal composition of $\text{Mn}_{1.02}\text{Co}_{0.98}\text{Si}$ by arc melting under Ar atmosphere. The samples were melted five times for homogeneity and 4 at. % extra Mn was introduced to compensate for the evaporation of Mn during melting. The as-cast ingots were sealed in quartz ampoules under 20 kPa Ar and annealed at 1123 K for 60 h. Then, the samples were slowly cooled to room temperature (RT) over 72 h [37] in order to release the strain that develops during the martensitic transition [38,39] between the high-temperature hexagonal state and the orthorhombic ground state.

Zero-field differential scanning calorimetry (DSC) measurements were carried out using a commercial TA-Q2000 DSC calorimeter. X-ray diffraction (XRD) patterns at different temperatures were collected using an Anton Paar TTK450 temperature-tunable sample chamber and a PANalytical Xpert Pro diffractometer with Cu $K\alpha$ radiation. The XRD patterns were processed using FULLPROF's implementation of the Rietveld refinement method [40]. Temperature-dependent magnetization (M - T) and field-dependent magnetization (M - H) curves below 7 T were measured in a superconducting quantum interference device (SQUID, Quantum Design MPMS 7XL) magnetometer. The corresponding curves up to 14 T were obtained from a physical properties measurement system (PPMS 14 T, Quantum Design).

Direct measurements of the adiabatic temperature change ΔT_{ad} and the magnetization at different temperatures and magnetic fields were performed simultaneously in a purpose-built experimental setup. Pulsed magnetic fields up to 40 T were provided by the Dresden High Magnetic Field Laboratory (HLD). The selected fields are 5, 10, 20, and 40 T, and the total pulse duration is around 160 ms. The temperature change was monitored by a carefully intertwined copper-constantan thermocouple (open loops induce a parasitic signal due to the field change [31]), which was squeezed between two plate-shaped samples to optimize the thermal contact and reduce the heat losses. The sample-thermometer geometry was enclosed in a thin-walled vacuum tube to provide better adiabatic conditions. The target temperature was controlled with a local heater. Resistive Pt-100 (high temperature) and Cernox (low temperature) thermometers were utilized to determine the reference temperature. The magnetization was measured in a home-built pulsed-field magnetometer similar to Ref. [25] by integrating the voltage induced in compensated pick-up coils surrounding the sample. The absolute values of the magnetization were calibrated against the lower-field data from the PPMS.

III. RESULTS AND DISCUSSION

In Fig. 1(a) the results from XRD measurements on the $\text{Mn}_{1.02}\text{Co}_{0.98}\text{Si}$ compound are shown for temperatures between room temperature (RT) and 443 K. The main (112), (202), (211), and (103) reflections show minor shifts for increasing temperature. As in Fig. 1(b), a Rietveld refinement of the XRD patterns confirms the orthorhombic $Pnma$ (space group 62) crystal structure, where Mn, Co, and Si atoms are positioned at three different $4c$ sites. No impurity phases were observed. In Fig. 1(c), the lattice parameters between RT and 363 K (gray area) exhibit anisotropic lattice distortions; for instance, the lattice along a shows a negative thermal expansion (-0.02%), whereas b and c have conventional expansions. When the temperature is above 363 K the lattice parameters increase roughly linearly with temperature (constant coefficients of linear thermal expansion). Figure 1(d) shows the unit-cell volume V as a function of the temperature. The experimental behavior is in agreement with other experimental observations [22,41]. The anisotropic changes in the lattice structure are associated with the strong magnetoelastic coupling. A similar behavior was observed in the hexagonal $(\text{Mn}, \text{Fe})_2(\text{P}, \text{Si})$ -based MCMs [42], where lattice parameter a shrinks (negative thermal expansion) and lattice parameters b and c expand (conventional positive thermal expansion). The derived lattice parameters a , b , c and the unit-cell volume V for the $\text{Mn}_{1.02}\text{Co}_{0.98}\text{Si}$ compound at different temperatures are summarized in Table S1 (Supplemental Material) [43].

It is known that the MnCoSi system exhibits a metamagnetic transition below its Néel temperature (T_N). As shown in Fig. S1 (Supplemental Material) [43] the Néel temperature for the $\text{Mn}_{1.02}\text{Co}_{0.98}\text{Si}$ compound corresponds to $T_N = 380.4$ K. In Fig. 2(a), the isothermal M - T curves under static conditions suggest that the tricriticality of the metamagnetic transition is observed because it is initially second order, but becomes first order for increasing applied magnetic fields. Combining neutron diffraction (ND) and density functional theory (DFT) calculations, Barcza *et al.* [22] proposed that this phenomenon is mainly controlled by the nearest-neighbor Mn-Mn distance. This metamagnetic transition couples with the change in the nearest Mn-Mn distance, where the low-temperature noncollinear antiferromagnetism is gradually suppressed in applied magnetic fields. It is interesting to note that, as shown in Fig. S2(a) (Supplemental Material) [43], the thermal hysteresis (ΔT_{hys}) continuously increases with increasing field and that the field dependence of the transition temperature $dT_t/d\mu_0 H$ gradually decreases with field from -60 K/T (2–3 T), -23 K/T (3–5 T), -15 K/T (5–7 T), and -13 K/T (7–10 T) to -10 K/T (10–14 T), respectively. Note that the large $dT_t/d\mu_0 H$ shift in low fields could result from the competition between antiferromagnetic and ferromagnetic ordering [10]. Therefore, it is worthwhile to further investigate (i) how T_t changes in higher magnetic fields (especially pulsed fields) and establish the phase diagram of T_t , and (ii) the behavior of this magnetoelastic metamagnetic transition. Based on the Maxwell relation $\Delta S_m(T, H) = \int_0^H \left(\frac{\partial M}{\partial T} \right)_H d\mu_0 H$, the magnetic entropy change ΔS_m with different magnetic-field changes ($\Delta\mu_0 H$) is estimated for the $\text{Mn}_{1.02}\text{Co}_{0.98}\text{Si}$ compound. Figure 2(b) shows the magnetic entropy change derived under

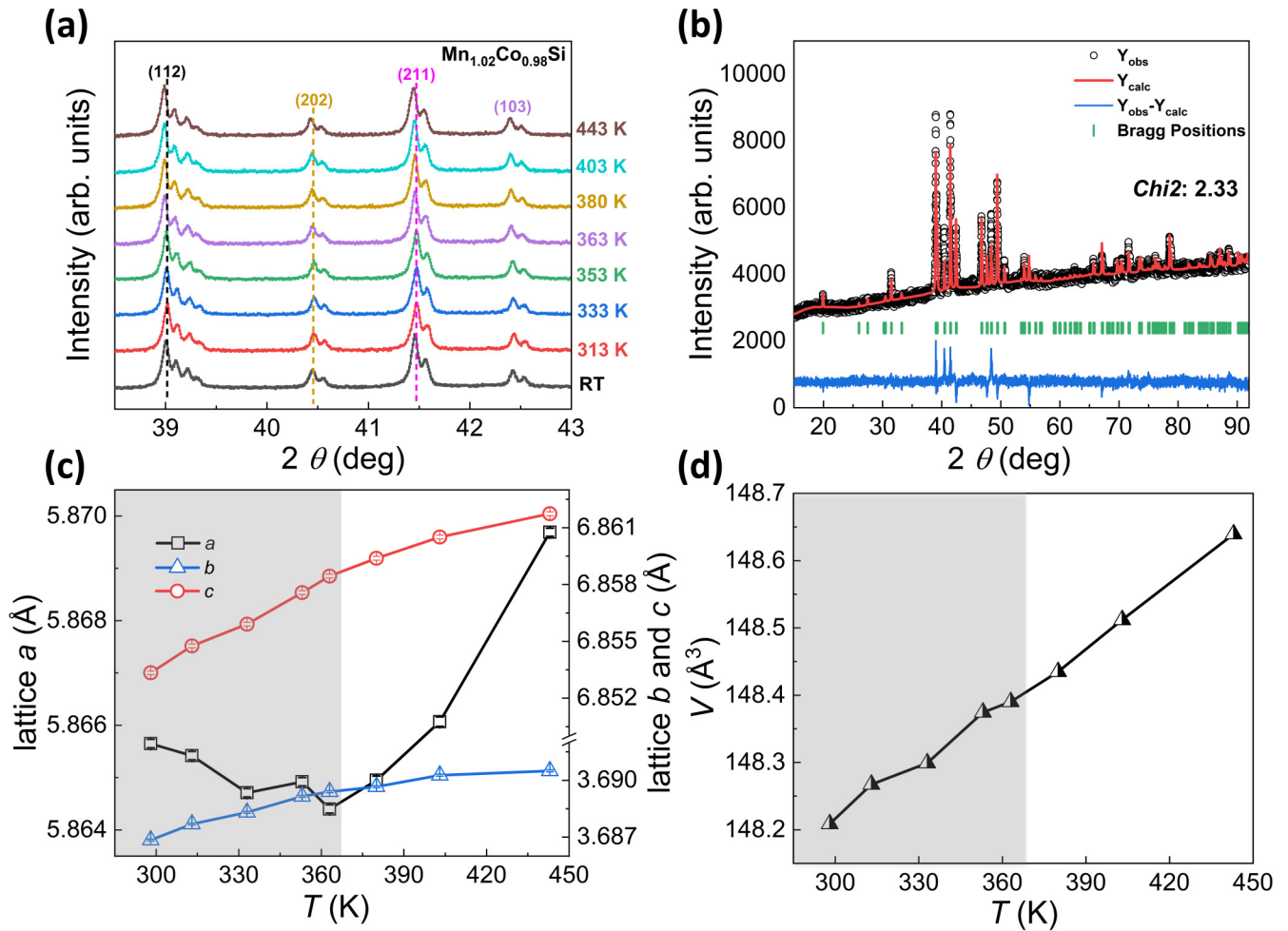


FIG. 1. (a) XRD patterns for the orthorhombic Mn_{1.02}Co_{0.98}Si compound measured at different temperatures. (b) Rietveld refinement of the XRD pattern at 313 K. (c) Derived lattice parameters and (d) unit-cell volume as a function of the temperature for the Mn_{1.02}Co_{0.98}Si compound.

isothermal conditions, resulting in a moderate MCE performance consistent with previous studies [10,44]. The signs of ΔS_m change when the inverse and conventional MCE compensate each other at around 330 K.

The adiabatic temperature change ΔT_{ad} , which is another key parameter for the MCE performance, is directly estimated from the pulsed field experiments at different temperatures and magnetic fields, as shown in Figs. 3(a)–3(d). The negative ΔT_{ad} values are characteristic for the inverse MCE. A distinct feature of these ΔT_{ad} - H curves is the asymmetric shape for the up-sweeping magnetization and down-sweeping demagnetization processes. This asymmetry could be ascribed to the faster pulse rates for the up-sweeping compared to the down-sweeping curves. This difference is expected to affect the nucleation and growth of the phase forming in the MnCoSi compound. Martensitic and ferroelastic first-order transitions are dominated by nucleation-growth processes that typically occur in the ultrasonic frequency range between kHz and MHz [45]. As shown in Fig. S3(b) (Supplemental Material) [43] the rate for the up-sweeping process (up to 6000 T/s for 40 T) is significantly higher than the down-sweeping process. That will cause a kinetic effect with a residual fraction of the parent phase. A similar effect was observed in NiMn-based magnetic

Heusler compounds [34,35] and in FeRh ferromagnets [32]. As demonstrated in Figs. 3(e)–3(h) it is found that the peaks in $|\Delta T_{ad}|$ roughly match the field-time profile of the pulsed fields when the measured temperature is close to the AFM-FM transition. The close similarity between the starting points for $|\Delta T_{ad}|$ and the pulsed fields indicates the good adiabatic experimental condition. In Fig. 4(a) the direct ΔT_{ad} measurement setup is schematically illustrated. It should be noted that for the adiabatic MCE measurement (no delay in response between the sample and the thermocouple) a requirement of the setup is to satisfy the following condition: $\tau_t \leq \Delta t \leq \tau_b$, where τ is the thermal time constant ($\tau_b = C_s/\kappa_b$ and $\tau_t = C_t/\kappa_t$), C is the heat capacity, κ is the thermal conductivity, and Δt is the duration of the field pulse [46]. Note that index b refers to the link of the sample with the thermal bath and index t refers to the link of the sample with the temperature sensor [see Fig. 4(a)]. A more detailed discussion can be found in the Supplemental Material [43]. Additionally, it is worth pointing out that $|\Delta T_{ad}|$ is only partially reversible for the highest pulsed fields with $\Delta\mu_0 H = 40$ T (highest sweep rate).

As mentioned before, in comparison to other strong magnetoelastic systems such as (Mn, Fe)₂(P, Si) based

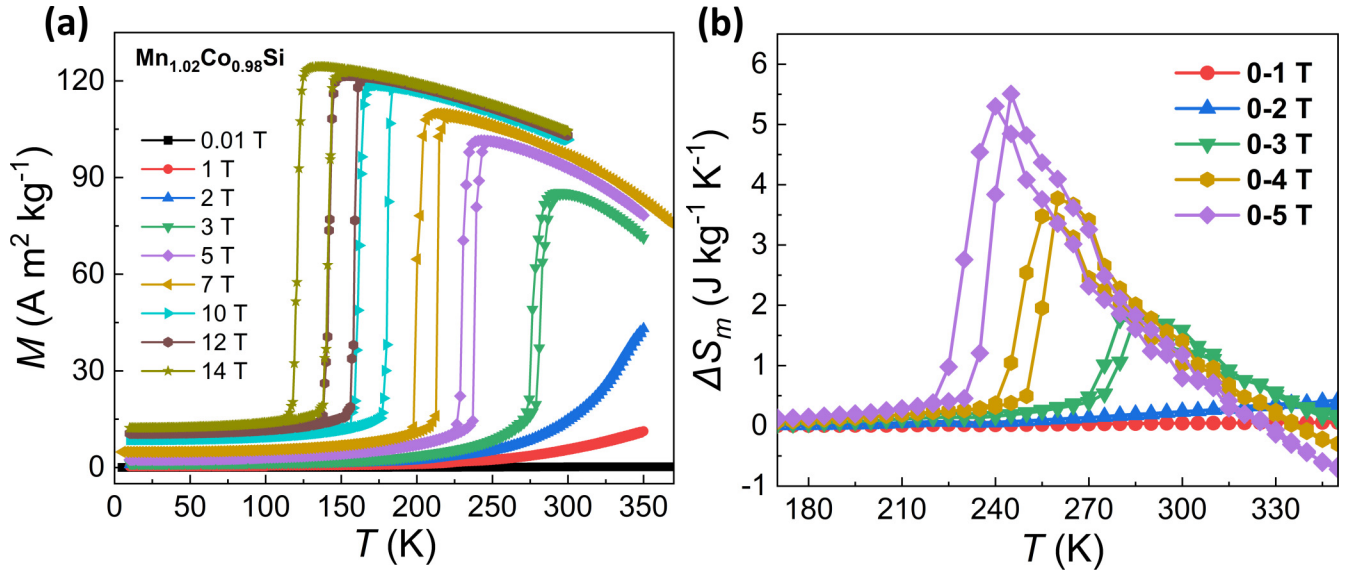


FIG. 2. (a) M - T curves for $\text{Mn}_{1.02}\text{Co}_{0.98}\text{Si}$ compound measured in different magnetic fields. (b) Magnetic entropy change ΔS_m for $\text{Mn}_{1.02}\text{Co}_{0.98}\text{Si}$ as a function of the temperature for both heating and cooling, determined in a magnetic-field change $\Delta\mu_0 H$ ranging from 1 to 5 T.

(+3 to 4 K/T) [6], $\text{La}(\text{Fe}, \text{Si})_{13}$ based (+4.5 K/T) [47], and FeRh-based (−8.5 K/T) [48] compounds, the $\text{Mn}_{1.02}\text{Co}_{0.98}\text{Si}$ sample holds a large magnitude of $dT_i/d\mu_0 H$ (high sensitivity of T_i on the applied magnetic field) with values that exceed −50 K/T for low-field changes (2–3 T) and values that exceed −10 K/T for high-field changes (10–14 T). Although the MCE will exist within a wide range of working temperatures, however, the corresponding $|\Delta T_{\text{ad}}|$ will be significantly degraded as a function of temperature, as well as the ΔS_m [as in Fig. 2(b)] because of the $\Delta S_m \propto (dT_i/d\mu_0 H)^{-1}$ (Clausius-Clapeyron) relation [10]. In addition, it is suggested that the ΔT_{ad} extracted in Fig. 3 might be the combination of the inverse and the conventional MCE and it will compensate the magnitude of MCE. In Fig. 4(b) the maximum $|\Delta T_{\text{ad}}|$ values $\Delta T_{\text{ad}}^{\text{max}}$ of the $\text{Mn}_{1.02}\text{Co}_{0.98}\text{Si}$ sample are mapped for different temperatures and fields indicating a maximum value of $|\Delta T_{\text{ad}}| \simeq 3.1$ K with $\Delta\mu_0 H \simeq 13$ T. Note that $\Delta T_{\text{ad}}^{\text{max}}$ is derived from the down-sweeping demagnetization process, as ΔT_{ad} measurements are generally pulse rate dependent [34].

As illustrated in Figs. 5(a)–5(d), the magnetization changes of the $\text{Mn}_{1.02}\text{Co}_{0.98}\text{Si}$ compound as a function of different pulsed fields are obtained for temperatures between 18 K and RT. In Fig. 5(a) it is observed that in low-magnetic fields (e.g., 1 T), the sample presents a weak magnetization, whereas it approaches a strong ferromagnetic state with increasing magnetic fields when the metamagnetic transition takes place.

The continuous increase in magnetic hysteresis ($\Delta\mu_0 H_{\text{hys}}$) for decreasing temperature means that the transition strengthens its first-order character at lower temperatures. Note that, compared with the M - H curves under isothermal conditions shown in Fig. S2(b) (Supplemental Material) [43], the curves obtained under adiabatic conditions are slightly different, originating in the difference in the effective temperature in both conditions [33,49]. The decrease in magnetization at low temperatures in Figs. 5(a) and 5(b) suggests that the incomplete transition needs higher magnetic fields than

the maximum applied values of 5 and 10 T, respectively. As presented in Fig. 5(c), the field-driven metamagnetic transition gradually moves to lower temperatures (down to 110 K) when a maximum pulsed field of 20 T is applied. The lower temperatures are accompanied by an enhanced M_s (up to $126 \text{ A m}^2 \text{ kg}^{-1}$). However, in Fig. 5(d) it is observed that upon pulsing to 40 T, the metamagnetic transition reaches a limit and no more movement is observed at the lowest temperatures ranging from 33 to 18 K. Also M_s does not increase any more at the lowest temperatures (below 33 K). Based on the above results, the critical magnetic-field $\mu_0 H_{\text{cr}}$, defined from the inflection point in the M - H curves [10], is extracted. In Fig. S4 (Supplemental Material) [43] the phase diagram with $\mu_0 H_{\text{cr}}$ versus the temperature is presented. It is found that (i) with decreasing temperature, the field hysteresis $\Delta\mu_0 H_{\text{hys}}$ between field-up (\uparrow) and field-down (\downarrow) critical fields increases; (ii) this change in the field hysteresis $\Delta\mu_0 H_{\text{hys}}$ shows a nonlinear temperature dependence: it changes slowly for temperatures above 200 K ($\mu_0 H_{\text{cr}} < 5$ T) and almost linearly between 100 and 200 K ($5 < \mu_0 H_{\text{cr}} < 18$ T) and saturates to an almost constant value below 100 K ($\mu_0 H_{\text{cr}} > 8$ T). At the lowest measurement temperature of 18.2 K the values of $\mu_0 H_{\text{cr}}$ of field-up (\uparrow) and field-down (\downarrow) pulses are 22.3 and 20.3 T, respectively. The values for the critical field for the metamagnetic transition $\mu_0 H_{\text{cr}}$ in the $\text{Mn}_{1.02}\text{Co}_{0.98}\text{Si}$ compound are listed in Table S2 (Supplemental Material) [43]. To investigate the dynamics of the magnetization process, the pulse time dependent magnetization is presented in Figs. 5(e) and 5(f) for different pulsed magnetic fields. It is apparent that the magnetization jumps during the up-sweeping magnetization process are steep, as it responds immediately when the external field exceeds the critical value. In contrast, the down-sweeping demagnetization process tends to be slower. The maximum (low-temperature) value of M_s for this $\text{Mn}_{1.02}\text{Co}_{0.98}\text{Si}$ compound corresponds to $130 \text{ A m}^2 \text{ kg}^{-1}$ at 18 K. The corresponding total magnetic moment obtained

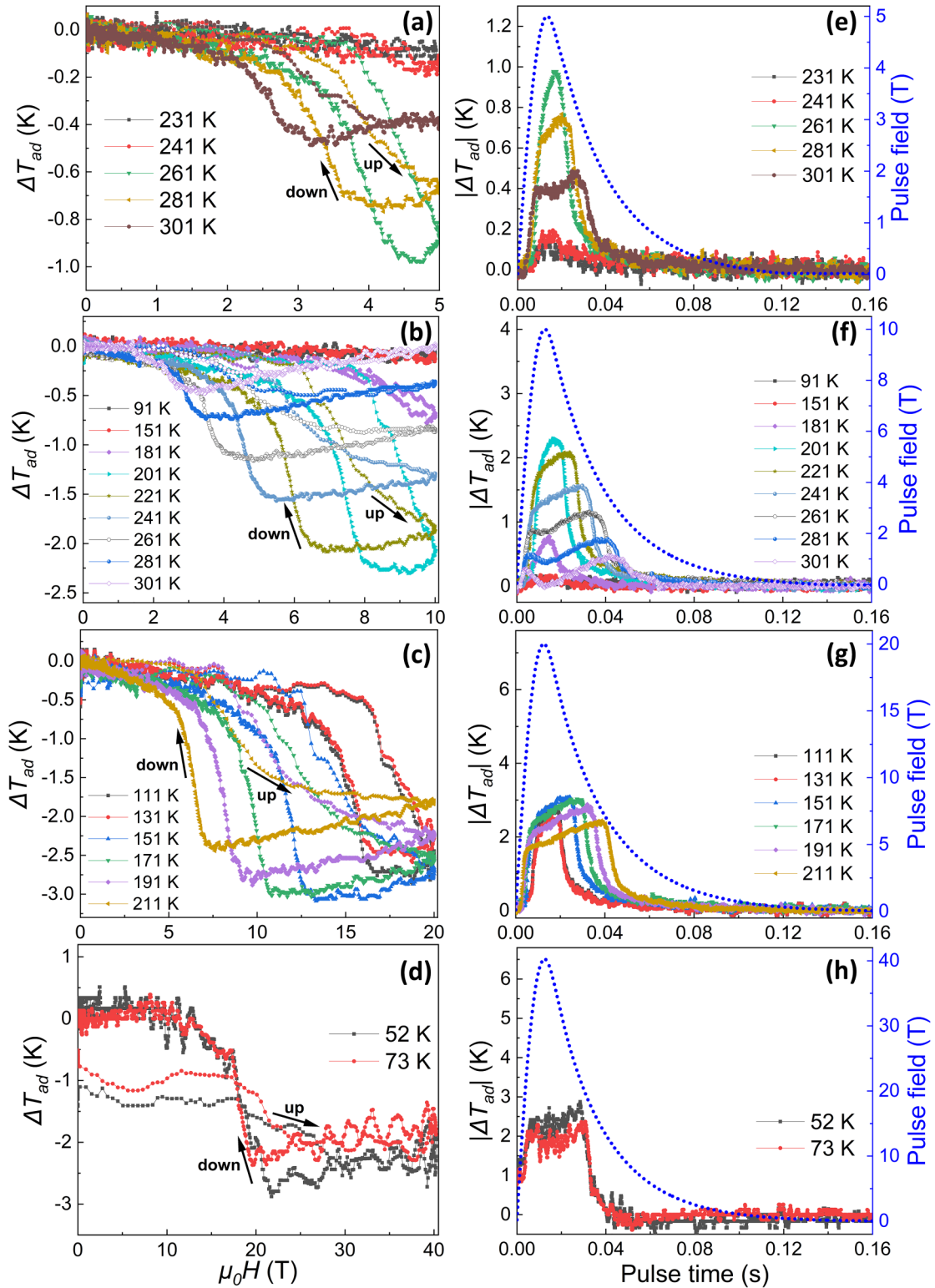


FIG. 3. Direct measurements of ΔT_{ad} for the $\text{Mn}_{1.02}\text{Co}_{0.98}\text{Si}$ compound at different temperatures as a function of the pulsed magnetic field in the following ranges: (a) 0–5 T, (b) 0–10 T, (c) 0–20 T, (d) 0–40 T. The corresponding absolute values of ΔT_{ad} as a function of the pulse time for the pulsed magnetic fields of (a)–(d) are presented in (e)–(h). The blue dashed lines are the pulsed magnetic-field profiles as a function of the pulse time.

from the pulse experiments is $3.3 \mu_B/\text{f.u.}$, which is in good agreement with the moment obtained from neutron diffraction at 4.2 K ($2.6 \mu_B$ for Mn and $0.4 \mu_B$ for Co) [50]. This indicates that all spins are completely aligned in the FM

state when the temperature is below 18 K and the field is beyond 22.3 T.

Combining the static- and pulse-field data, the phase diagram of T_i as a function of the applied magnetic field has

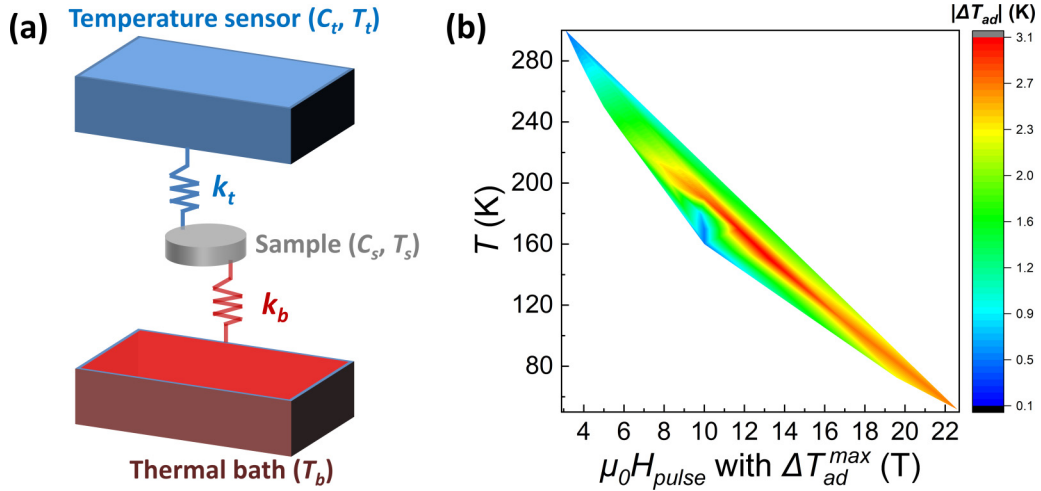


FIG. 4. (a) Schematic illustration of the direct ΔT_{ad} measurement setup. The bulk $\text{Mn}_{1.02}\text{Co}_{0.98}\text{Si}$ sample is coupled to the thermal bath and the temperature sensor by the thermal conductivity k_b and k_t , respectively. (b) 2D contour plot to map the maximum $|\Delta T_{ad}|$ value as a function of temperature and pulsed magnetic field. The scale bar represents the intensity of the $|\Delta T_{ad}|$ values.

been constructed for the $\text{Mn}_{1.02}\text{Co}_{0.98}\text{Si}$ compound, as shown in Fig. 6. As expected, the features of this phase diagram are like the phase diagram of $\mu_0 H_{cr}$ as a function of the temperature. In previous studies it was found that MnCoSi has a cycloidal spiral magnetic structure at low temperature ($T < 100$ K) and a helical magnetic structure at intermediate temperatures ($100 < T < 200$ K), as initially proposed [50] and later experimentally observed [41,51]. Upon applying a magnetic field, the magnetoelastic coupling starts to significantly grow at temperatures around 280 K and below. This is signaled by a field-driven AFM-FM metamagnetic transition accompanied with a structural elastic deformation (lattice parameter a shows an abnormal reduction with temperature in the temperature range from 200 to 300 K in zero field [41]). The stiffness of this magnetoelastic coupling strongly depends on a subtle change in the nearest Mn-Mn atomic distance ($d_{\text{Mn}}-d_{\text{Mn}}$) and the corresponding bonding angles [44]. Once the coupling is built, the metamagnetic transition will take place at the tricritical point. The thermal hysteresis ΔT_{hys} of the metamagnetic transition increases with the magnetic field increasing. For higher fields, the temperature window of the anisotropic lattice deformation gradually shifts to lower temperature, as observed experimentally [22]. Thus, the ferromagnetism is enhanced in the applied magnetic field (inversely AFM is suppressed). This can be understood from the Clausius-Clapeyron equation:

$$\frac{dT_t}{d\mu_0 H} = -\frac{\Delta M}{\Delta S}, \quad (1)$$

where $dT_t/d\mu_0 H$ means the sensitivity of T_t on the external magnetic field, ΔS is the change in entropy, and ΔM is the change in magnetization at the transition. The value of $dT_t/d\mu_0 H \approx -10$ K/T is stable in static magnetic fields. The pulsed magnetic-field data in Figs. 5(e)–5(f) indicate the growth of the saturation magnetization in growing applied magnetic fields, indicating that the maximum ΔS can further increase in a broad range of temperatures. Furthermore, after crossing the almost linear acceleration stage in fields up to about 18 T, the metamagnetic transition between the AFM and

the FM state disappears for 20–25 T and only strong FM is present.

The above phenomenon can be understood in terms of the classical nucleation theory. Note that there is no time dependence for this material. This is the case for most field-induced transitions, but can be observed in systems such as maraging steels [52]. For a transition from the matrix phase α to the forming phase β , the change in Gibbs free energy of the system can be expressed as [53]

$$\Delta G = -V_\beta \Delta g_v + A_{\alpha\beta} \gamma_{\alpha\beta}, \quad (2)$$

where V_β is the volume of the formed phase β , Δg_v is the difference in Gibbs free energy between the forming phase β and the matrix phase α (chemical driving force), $A_{\alpha\beta}$ is the α/β interfacial area, and $\gamma_{\alpha\beta}$ is the α/β interfacial energy. If $\gamma_{\alpha\beta}$ is isotropic and the phase has a spherical shape with a radius r , then

$$\Delta G = -\frac{4}{3}\pi r^3 \Delta g_v + 4\pi r^2 \gamma_{\alpha\beta}, \quad (3)$$

where the first energy term results from the chemical driving force and the second term from the interfacial energy. To form a stable phase, the system needs to overcome an energy barrier. It is reached when $d\Delta G/dr = 0$. The energy barrier for nucleation is located at a critical radius r^* and has a value of ΔG^* which corresponds to

$$\Delta G^* = \frac{16\pi \gamma_{\alpha\beta}^3}{3(\Delta g_v)^2}. \quad (4)$$

For phase transitions with a limited undercooling ($\Delta T = T_e - T$, where T_e is the equilibrium transition temperature), Δg_v at nonequilibrium conditions is derived as

$$\Delta g_v \simeq L - T \frac{L}{T_e} \simeq \Delta S(T_e - T) \simeq \Delta S \Delta T, \quad (5)$$

where L is the latent heat and ΔS is the entropy change of the transition.

In the current pulsed field experiments, it is observed that with increasing field and decreasing temperature ΔS

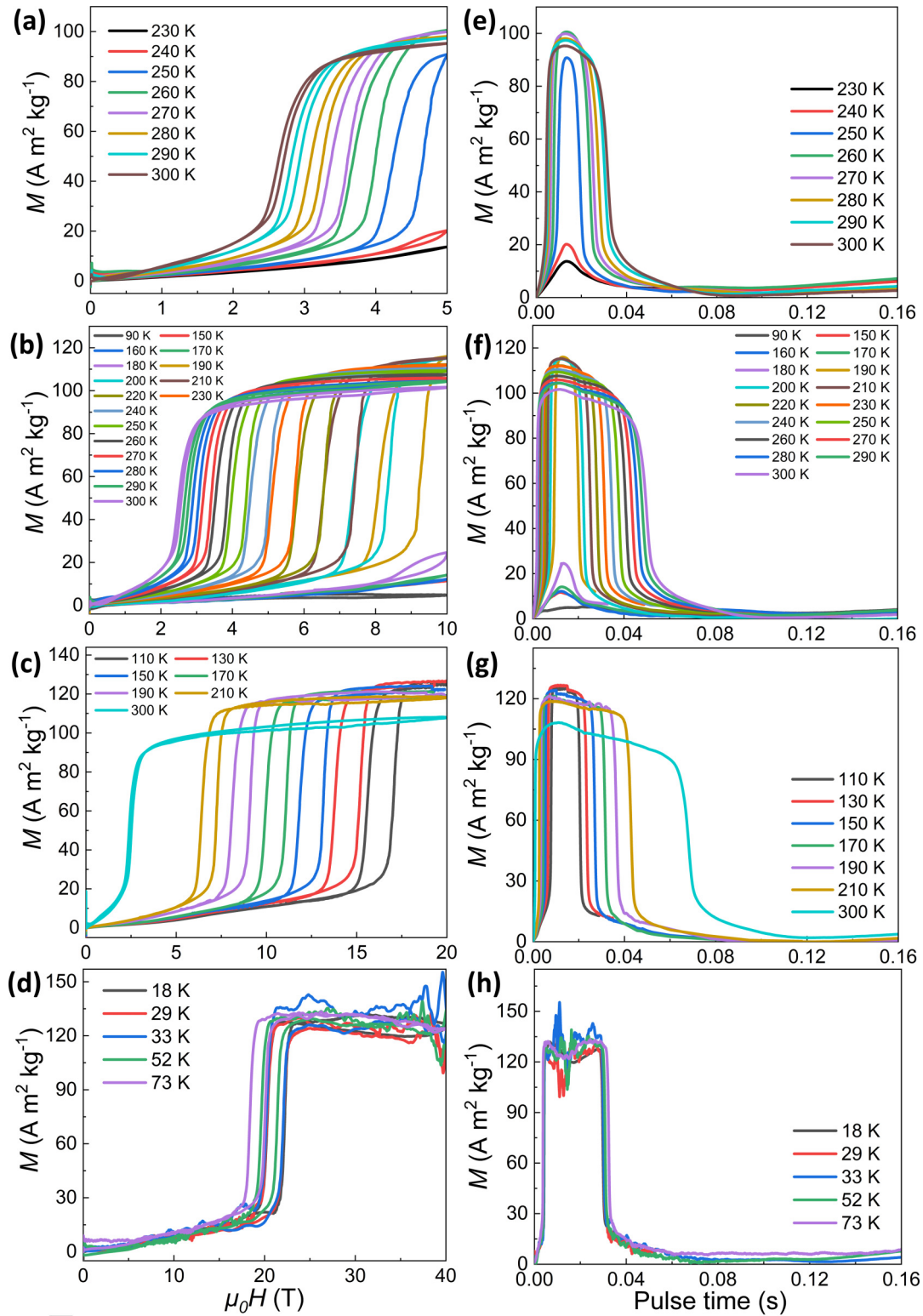


FIG. 5. Magnetization of the $\text{Mn}_{1.02}\text{Co}_{0.98}\text{Si}$ compound at different temperatures for pulsed magnetic-field ranges of (a) 0–5 T, (b) 0–10 T, (c) 0–20 T, (d) 0–40 T. The magnetization curves corresponding to the field curves of (a)–(d) during the magnetizing and demagnetizing processes as a function of pulse time are presented in (e)–(h).

decreases and tends to zero (no transition happens). This suggests that the energy barrier for nucleation ΔG^* increases at low temperatures, which suppresses the spontaneous evolution of the transition. The probability per unit of time that

the host atoms cross the energy barrier for nucleation and create a stable cluster of the forming phase (nucleation rate) is proportional to $\exp(-\Delta G^*/k_B T)$, where k_B is the Boltzmann constant. Considering that at low temperatures Δg_v , and

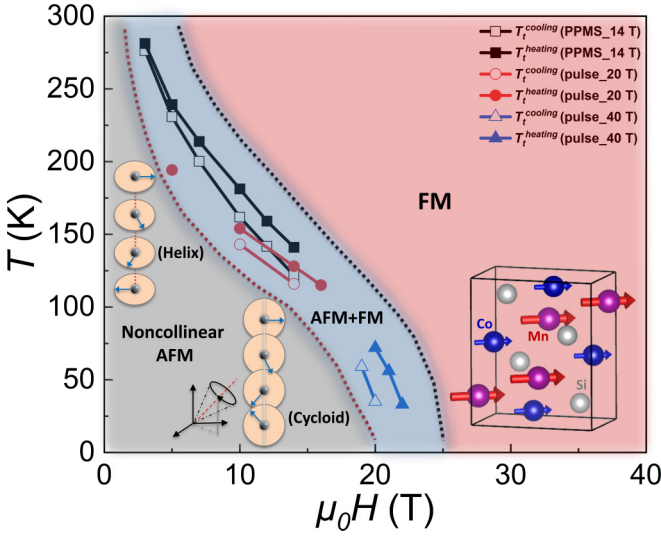


FIG. 6. Phase diagram T - $\mu_0 H$ constructed from T_i as a function of the applied magnetic field $\mu_0 H$ (combining the static and pulse fields) for the $\text{Mn}_{1.02}\text{Co}_{0.98}\text{Si}$ compound. The inset shows the highly crystal-ordered orthorhombic structure for the MnCoSi material system.

thereby also ΔG^* is stabilized, the factor $\exp(-\Delta G^*/k_B T)$ strongly decreases for decreasing temperature T . This reduction in nucleation rate effectively suppresses the transition.

It is expected that the stabilization of the chemical driving force occurs in the temperature range where the density of thermally excited phonons is strongly reduced. According to the Debye model [54], the specific heat C_p versus temperature shows a maximum slope around $0.28\theta_D$, where θ_D is the Debye temperature [54,55]. For MnCoSi and related derivatives θ_D is between 375 and 385 K [56,57], resulting in a maximum slope around 100 K. For temperatures below $0.1\theta_D$ (about 40 K), the amount of thermally excited phonons is very low, which is consistent with our experimental observation (no transition).

Metamagnetic AFM-FM and AFM-ferrimagnetic (FI) transitions have been found for FeRh-based [58] and Mn_2Sb -based magnetocaloric materials [59]. In these cases a nonlinear dependence is observed between the critical field ($\mu_0 H_{\text{cr}}$) and temperature. It was found that the transition field can be described by the following quadratic expression [58],

$$\mu_0 H_{\text{cr}} = \alpha[1 - (T/T_c)^2], \quad (6)$$

where α is a constant. The authors proposed that the quadratic temperature dependence of $\mu_0 H_{\text{cr}}(T)$ is typical for first-order magnetic phase transitions of electronic origin. A similar quadratic temperature dependence of $\mu_0 H_{\text{cr}}$ has also been observed in Ni-doped FeRh materials in high magnetic fields [60]. Therefore, to check whether the metamagnetic transition (AFM-FM) follows a similar behavior in our MnCoSi itinerant electron system [61], we applied the following relation,

$$\mu_0 H_{\text{cr}} = a - bT^n, \quad (7)$$

where a , b , and n are constants. As shown in Fig. S5 (Supplemental Material) [43], when the temperature is below 200 K, the fitting closely follows Eq. (7) with $a = 21.0(2)$,

$b = 0.0034(4)$, and $n = 1.57(7)$ ($R^2 = 0.998$). This indicates that for this system the temperature dependence of $\mu_0 H_{\text{cr}}$ corresponds to a temperature exponent of $n = 3/2$ for MnCoSi rather than the $n = 2$ found for FeRh and Mn_2Sb compounds. This could result from the complexity of this noncollinear AFM structure and the spin fluctuations at low temperature in the MnCoSi materials. As mentioned before, the system shows a spin-flip transition from a cycloid AFM to a helix AFM, and then finally to an ordered FM state. The present findings provide useful insight in the magnetic structure evolution in high fields.

In addition, according to the thermal activation model, previously applied for FeRh compounds [62], it is proposed that the temperature dependence of field hysteresis ($\mu_0 \Delta H_{\text{cr}}$) can be described by the expression [58]

$$\mu_0 \Delta H_{\text{cr}} = \mu_0 \Delta H_{\text{cr}}^0 (1 - cT^{\frac{1}{2}}), \quad (8)$$

where H_{cr}^0 and c are constants. However, as shown in Fig. S6 (Supplemental Material) [43], for our case it is found that the hysteresis in the critical magnetic field closely follows a linear relation with temperature.

IV. CONCLUSIONS

The magnetocaloric effect in polycrystalline $\text{Mn}_{1.02}\text{Co}_{0.98}\text{Si}$, which originates from a large magnetoelastic coupling, has been studied in terms of its structural, caloric, and magnetic behavior. Pulsed magnetic-field measurements up to fields of 40 T present a moderate ΔT_{ad} for MnCoSi, which is related to a metamagnetic transition that is induced in external magnetic fields. The applied magnetic field strengthens the strong magnetoelastic coupling, which is signaled by an increase in M_s . For decreasing temperature, the metamagnetic transition between the AFM and FM state saturates at a critical field $\mu_0 H_{\text{cr}}$ between 20 and 25 T. Above this critical field, all spins of magnetic atoms (Mn and Co) are fully aligned. The phase diagram, mapping the critical temperature T_i and the critical field $\mu_0 H_{\text{cr}}$, has been constructed for the whole accessible temperature and field range. Additionally, we explain the saturation of $\mu_0 H_{\text{cr}}$ at low temperatures in terms of the energy barrier for nucleation. This study reveals how the strong magnetoelastic coupling changes under pulsed magnetic fields in a representative MnCoSi sample, which provides unique insights in these MCMs and their behavior in high magnetic fields.

ACKNOWLEDGMENTS

The authors thank Anton Lefering, Bert Zwart, Robert Dankelman, and Michel Steenvoorden for their technical assistance. This work was financially supported by NWO in the domain of the Applied and Engineering Sciences (AES) program and the China Scholarship Council. F.Z. thanks Dr. Jun Liu (NJUST) for fruitful discussion. We gratefully acknowledge the financial support by the HLD at HZDR, member of the European Magnetic Field Laboratory (EMFL), the Helmholtz Association via the Helmholtz-RSF Joint Research Group (Project No. HRSF-0045), and the Deutsche Forschungsgemeinschaft (DFG, German Research Foundation) within the project BEsT (Project-ID No. 456263705).

- [1] E. R. Callen and H. B. Callen, Static magnetoelastic coupling in cubic crystals, *Phys. Rev.* **129**, 578 (1963).
- [2] O. Tegus, E. Brück, K. H. J. Buschow, and F. R. de Boer, Transition-metal-based magnetic refrigerants for room-temperature applications, *Nature (London)* **415**, 150 (2002).
- [3] N. H. Dung, Z. Q. Ou, L. Caron, L. Zhang, D. T. C. Thanh, G. A. de Wijs, R. A. de Groot, K. H. J. Buschow, and E. Brück, Mixed magnetism for refrigeration and energy conversion, *Adv. Energy Mater.* **1**, 1215 (2011).
- [4] S. Lee, A. Pirogov, M. S. Kang, K. H. Jang, M. Yonemura, T. Kamiyama, S. W. Cheong, F. Gozzo, N. Shin, H. Kimura, Y. Noda, and J. G. Park, Giant magneto-elastic coupling in multiferroic hexagonal manganites, *Nature (London)* **451**, 805 (2008).
- [5] M. Chandra, S. Yadav, R. J. Choudhary, R. Rawat, A. K. Sinha, M. B. Lepetit, and K. Singh, Multiferroicity and magnetoelastic coupling in α -Mn₂O₃: A binary perovskite, *Phys. Rev. B* **98**, 104427 (2018).
- [6] F. Guillou, G. Porcari, H. Yibole, N. van Dijk, and E. Brück, Taming the first-order transition in giant magnetocaloric materials, *Adv. Mater.* **26**, 2671 (2014).
- [7] F. X. Hu, B. G. Shen, J. R. Sun, Z. H. Cheng, G. H. Rao, and X. X. Zhang, Influence of negative lattice expansion and metamagnetic transition on magnetic entropy change in the compound LaFe_{11.4}Si_{1.6}, *Appl. Phys. Lett.* **78**, 3675 (2001).
- [8] E. Stern-Taulats, A. Planes, P. Lloveras, M. Barrio, J. L. Tamarit, S. Pramanick, S. Majumdar, C. Frontera, and L. Mañosa, Barocaloric and magnetocaloric effects in Fe₄₉Rh₅₁, *Phys. Rev. B* **89**, 214105 (2014).
- [9] F. Guillou, A. K. Pathak, D. Paudyal, Y. Mudryk, F. Wilhelm, A. Rogalev, and V. K. Pecharsky, Non-hysteretic first-order phase transition with large latent heat and giant low-field magnetocaloric effect, *Nat. Commun.* **9**, 2925 (2018).
- [10] K. G. Sandeman, R. Daou, S. Ozcan, J. H. Durrell, N. D. Mathur, and D. J. Fray, Negative magnetocaloric effect from highly sensitive metamagnetism in CoMnSi_{1-x}Ge_x, *Phys. Rev. B* **74**, 224436 (2006).
- [11] X. Moya and N. D. Mathur, Caloric materials for cooling and heating, *Science* **370**, 797 (2020).
- [12] H. Johra, K. Filonenko, P. Heiselberg, C. Veje, S. Dall'Olio, K. Engelbrecht, and C. Bahl, Integration of a magnetocaloric heat pump in an energy flexible residential building, *Renewable Energy* **136**, 115 (2019).
- [13] T. Christiaanse and E. Brück, Proof-of-concept static thermomagnetic generator experimental device, *Metall. Mater. Trans. E* **1**, 36 (2014).
- [14] A. Waske, D. Dzekan, K. Sellschopp, D. Berger, A. Stork, K. Nielsch, and S. Fähler, Energy harvesting near room temperature using a thermomagnetic generator with a pretzel-like magnetic flux topology, *Nat. Energy* **4**, 68 (2019).
- [15] D. Dzekan, A. Waske, K. Nielsch, and S. Fähler, Efficient and affordable thermomagnetic materials for harvesting low grade waste heat, *APL Mater.* **9**, 011105 (2021).
- [16] J. O'Donnell, M. S. Rzechowski, J. N. Eckstein, and I. Bozovic, Magnetoelastic coupling and magnetic anisotropy in La_{0.67}Ca_{0.33}MnO₃ films, *Appl. Phys. Lett.* **72**, 1775 (1998).
- [17] F. Theuss, S. Ghosh, T. S. Chen, O. Tchernyshyov, S. Nakatsuji, and B. J. Ramshaw, Strong magnetoelastic coupling in Mn₃X (X = Ge, Sn), *Phys. Rev. B* **105**, 174430 (2022).
- [18] V. Johnson and C. G. Frederic, Magnetic and crystallographic properties of ternary manganese silicides with ordered Co₂P structure, *Phys. Status Solidi A* **20**, 331 (1973).
- [19] S. Niziol, H. Bińczycka, A. Szytula, J. Todorović, R. Fruchart, J. P. Senateur, and D. Fruchart, Structure magnétique des MnCoSi, *Phys. Status Solidi* **45**, 591 (1978).
- [20] S. Niziol, R. Fruchart, and J. P. Senateur, Magnetic-properties of CoMnSi and CoMnSi_{0.85}Ge_{0.15}, *Phys. Status Solidi A* **51**, K23 (1979).
- [21] A. Barcza, Z. Gercsi, K. S. Knight, and K. G. Sandeman, Giant Magnetoelastic Coupling in a Metallic Helical Metamagnet, *Phys. Rev. Lett.* **104**, 247202 (2010).
- [22] A. Barcza, Z. Gercsi, H. Michor, K. Suzuki, W. Kockelmann, K. S. Knight, and K. G. Sandeman, Magnetoelastic coupling and competing entropy changes in substituted CoMnSi metamagnets, *Phys. Rev. B* **87**, 064410 (2013).
- [23] C. S. Mejia, M. G. Zavareh, A. K. Nayak, Y. Skourski, J. Wosnitza, C. Felser, and M. Nicklas, Pulsed high-magnetic-field experiments: New insights into the magnetocaloric effect in Ni-Mn-In Heusler alloys, *J. Appl. Phys.* **117**, 17E710 (2015).
- [24] M. G. Zavareh, C. S. Mejia, A. K. Nayak, Y. Skourski, J. Wosnitza, C. Felser, and M. Nicklas, Direct measurements of the magnetocaloric effect in pulsed magnetic fields: The example of the Heusler alloy Ni₅₀Mn₃₅In₁₅, *Appl. Phys. Lett.* **106**, 071904 (2015).
- [25] Y. Skourski, M. D. Kuz'min, K. P. Skokov, A. V. Andreev, and J. Wosnitza, High-field magnetization of Ho₂Fe₁₇, *Phys. Rev. B* **83**, 214420 (2011).
- [26] S. Taskaev, V. Khovaylo, K. Skokov, W. Liu, E. Bykov, M. Ulyanov, D. Bataev, A. Basharova, M. Kononova, D. Plakhotkiy, M. Bogush, T. Gottschall, and O. Gutfleisch, Magnetocaloric effect in GdNi₂ for cryogenic gas liquefaction studied in magnetic fields up to 50 T, *J. Appl. Phys.* **127**, 233906 (2020).
- [27] E. Bykov, W. Liu, K. Skokov, F. Scheibel, O. Gutfleisch, S. Taskaev, V. Khovaylo, D. Plakhotkiy, C. S. Mejia, J. Wosnitza, and T. Gottschall, Magnetocaloric effect in the Laves-phase Ho_{1-x}Dy_xAl₂ family in high magnetic fields, *Phys. Rev. Mater.* **5**, 095405 (2021).
- [28] W. Liu, E. Bykov, S. Taskaev, M. Bogush, V. Khovaylo, N. Fortunato, A. Aubert, H. B. Zhang, T. Gottschall, J. Wosnitza, F. Scheibel, K. Skokov, and O. Gutfleisch, A study on rare-earth Laves phases for magnetocaloric liquefaction of hydrogen, *Appl. Mater. Today* **29**, 101624 (2022).
- [29] T. Gottschall, M. D. Kuz'min, K. P. Skokov, Y. Skourski, M. Fries, O. Gutfleisch, M. G. Zavareh, D. L. Schlagel, Y. Mudryk, V. Pecharsky, and J. Wosnitza, Magnetocaloric effect of gadolinium in high magnetic fields, *Phys. Rev. B* **99**, 134429 (2019).
- [30] L. Beyer, B. Weise, J. Freudenberger, J. K. Hufenbach, T. Gottschall, and M. Krautz, Evaluation of the effective temperature change in Gd-based composite wires assessed by static and pulsed-field magnetic measurements, *J. Magn. Magn. Mater.* **536**, 168115 (2021).
- [31] N. Maraytta, Y. Skourski, J. Voigt, K. Friese, M. G. Herrmann, J. Persson, J. Wosnitza, S. M. Salman, and T. Bruckel, Direct measurements of the magneto-caloric effect of MnFe₄Si₃ in pulsed magnetic fields, *J. Alloys Compd.* **805**, 1161 (2019).

- [32] A. P. Kamantsev, A. A. Amirov, Y. S. Koshkid'ko, C. S. Mejia, A. V. Mashirov, A. M. Aliev, V. V. Koledov, and V. G. Shavrov, Magnetocaloric effect in alloy $\text{Fe}_{49}\text{Rh}_{51}$ in pulsed magnetic fields up to 50 T, *Phys. Solid State* **62**, 160 (2020).
- [33] M. G. Zavareh, Y. Skourski, K. P. Skokov, D. Y. Karpenkov, L. Zvyagina, A. Waske, D. Haskell, M. Zhernenkov, J. Wosnitzer, and O. Gutfleisch, Direct Measurement of the Magnetocaloric Effect in $\text{La}(\text{Fe}, \text{Si}, \text{Co})_{13}$ Compounds in Pulsed Magnetic Fields, *Phys. Rev. Appl.* **8**, 014037 (2017).
- [34] T. Gottschall, K. P. Skokov, F. Scheibel, M. Acet, M. G. Zavareh, Y. Skourski, J. Wosnitzer, M. Farle, and O. Gutfleisch, Dynamical Effects of the Martensitic Transition in Magnetocaloric Heusler Alloys from Direct ΔT_{ad} Measurements under Different Magnetic-Field-Sweep Rates, *Phys. Rev. Appl.* **5**, 024013 (2016).
- [35] C. Salazar-Mejia, V. Kumar, C. Felser, Y. Skourski, J. Wosnitzer, and A. K. Nayak, Measurement-Protocol Dependence of the Magnetocaloric Effect in Ni-Co-Mn-Sb Heusler Alloys, *Phys. Rev. Appl.* **11**, 054006 (2019).
- [36] C. Salazar-Mejia, P. Devi, S. Singh, C. Felser, and J. Wosnitzer, Influence of Cr substitution on the reversibility of the magnetocaloric effect in Ni-Cr-Mn-In Heusler alloys, *Phys. Rev. Mater.* **5**, 104406 (2021).
- [37] Y. Y. Gong, J. Liu, G. Z. Xu, F. Xu, and D. H. Wang, Large reversible magnetostriction in B-substituted MnCoSi alloy at room temperature, *Scr. Mater.* **127**, 165 (2017).
- [38] J. W. Lai, Z. G. Zheng, H. Y. Yu, D. C. Zeng, F. M. Xiao, T. Sun, and R. H. Tang, Tuning magnetocaloric effect to near-room temperature for $\text{MnCo}_{1-x}\text{Ge}_{0.5}\text{Si}_{0.5}$ alloys, *J. Mater. Eng. Perform.* **26**, 2346 (2017).
- [39] J. H. Chen, Z. Y. Wei, E. K. Liu, X. Qi, W. H. Wang, and G. H. Wu, Structural and magnetic properties of $\text{MnCo}_{1-x}\text{Fe}_x\text{Si}$ alloys, *J. Magn. Magn. Mater.* **387**, 159 (2015).
- [40] H. M. Rietveld, A profile refinement method for nuclear and magnetic structures, *J. Appl. Crystallogr.* **2**, 65 (1969).
- [41] J. Liu, B. Ding, Y. Yao, X. K. Xi, Z. X. Cheng, J. L. Wang, C. W. Wang, G. H. Wu, and W. H. Wang, Coherent spin rotation-induced zero thermal expansion in MnCoSi -based spiral magnets, *npg Asia Mater.* **13**, 70 (2021).
- [42] F. Guillou, H. Yibole, N. H. van Dijk, and E. Brück, Effect of boron substitution on the ferromagnetic transition of $\text{MnFe}_{0.95}\text{P}_{2/3}\text{Si}_{1/3}$, *J. Alloys Compd.* **632**, 717 (2015).
- [43] See Supplemental Material at <http://link.aps.org/supplemental/10.1103/PhysRevB.107.214431>. Table S1 shows lattice parameters and the unit-cell volume for the compound at different temperatures. Figure S1 presents DSC curves for heating and cooling. Figure S2 shows magnetic-field dependence of T_i from static isothermal M - T measurements. (b) M - H curves up to 5 T in the temperature range from 190 to 320 K. Figure S3 presents (a) pulsed magnetic-field $\mu_0 H$ profiles as a function of the pulse time and (b) derived pulsed field $\mu_0 H$ sweep rates as a function of the pulse time. Table S2 shows critical fields at different temperatures for the compound. Figure S4 is the temperature dependence of the magnetic critical field on up- and down-sweeping. Table S3 shows transition temperature T_i for cooling and heating at different applied magnetic fields. Figure S5 shows the fitting of critical field during down-sweeping as a function of temperature extracted from Fig. S4. Figure S6 shows the fitting of field hysteresis as a function of temperature.
- [44] Y. Liu, Z. T. Xu, K. M. Qiao, H. B. Zhou, F. R. Shen, T. Z. Yang, J. Wang, T. Y. Ma, F. X. Hu, and B. G. Shen, Strengthened caloric effect in MnCoSi under combined applications of magnetic field and hydrostatic pressure, *J. Mater. Sci.* **56**, 20060 (2021).
- [45] A. Planes, L. Mañosa, and E. Vives, Acoustic emission in martensitic transformations, *J. Alloys Compd.* **577**, S699 (2013).
- [46] T. Kihara, Y. Kohama, Y. Hashimoto, S. Katsumoto, and M. Tokunaga, Adiabatic measurements of magneto-caloric effects in pulsed high magnetic fields up to 55 T, *Rev. Sci. Instrum.* **84**, 074901 (2013).
- [47] Y. Ouyang, M. X. Zhang, A. Yan, W. Wang, F. Guilloud, and J. Liu, Plastically deformed La-Fe-Si : Microstructural evolution, magnetocaloric effect and anisotropic thermal conductivity, *Acta Mater.* **187**, 1 (2020).
- [48] A. Chirkova, K. P. Skokov, L. Schultz, N. V. Baranov, O. Gutfleisch, and T. G. Woodcock, Giant adiabatic temperature change in FeRh alloys evidenced by direct measurements under cyclic conditions, *Acta Mater.* **106**, 15 (2016).
- [49] R. Z. Levitin, V. V. Snegirev, A. V. Kopylov, A. S. Lagutin, and A. Gerber, Magnetic method of magnetocaloric effect determination in high pulsed magnetic fields, *J. Magn. Magn. Mater.* **170**, 223 (1997).
- [50] O. L. Baumfeld, Magnetoelastic coupling and tricritical metamagnetism, Ph.D. thesis, Imperial College London, 2017.
- [51] B. Ding, J. Liu, H. Li, J. J. Liang, J. Chen, Z. F. Li, X. Li, X. K. Xi, Z. X. Cheng, J. L. Wang, Y. Yao, and W. H. Wang, Observation of short-period helical spin order and magnetic transition in a nonchiral centrosymmetric helimagnet, *Adv. Funct. Mater.* **32**, 2200356 (2022).
- [52] D. San Martín, N. H. van Dijk, E. Jiménez-Melero, E. Kampert, U. Zeitler, and S. van der Zwaag, Real-time martensitic transformation kinetics in maraging steel under high magnetic fields, *Mater. Sci. Eng.: A* **527**, 5241 (2010).
- [53] D. A. Porter and K. E. Easterling, *Phase Transformations in Metals and Alloys* (CRC Press, Boca Raton, FL, 2009).
- [54] N. W. Ashcroft and N. D. Mermin, *Solid State Physics* (Cengage Learning, Boston, 1976).
- [55] J. Biele, M. Grott, M. E. Zolensky, A. Benisek, and E. Dachs, The specific heat of astro-materials: Review of theoretical concepts, materials, and techniques, *Int. J. Thermophys.* **43**, 144 (2022).
- [56] S. V. Syrotyuk, Electronic structure, magnetic and mechanical properties of MnCoSi half-Heusler alloy, *Metallofiz. Noveishie Tekhnol.* **43**, 541 (2021).
- [57] M. B. Gamza, W. Schnelle, H. Rosner, S. V. Ackerbauer, Y. Grin, and A. Leithe-Jasper, Complex magnetic phase diagram of metamagnetic MnPtSi , *Phys. Rev. B* **100**, 014423 (2019).
- [58] N. V. Baranov and E. A. Barabanova, Electrical-resistivity and magnetic phase-transitions in modified FeRh compounds, *J. Alloys Compd.* **219**, 139 (1995).
- [59] N. V. Baranov, Y. A. Khrulev, M. I. Bartashevich, T. Goto, and H. A. Katori, High-field magnetization process in $\text{Mn}_{1.9}\text{Cr}_{0.1}\text{Sb}$, *J. Alloys Compd.* **210**, 197 (1994).
- [60] A. M. Chirkova, K. P. Skokov, Y. Skourski, F. Scheibel, A. Y. Karpenkov, A. S. Volegov, N. V. Baranov, K. Nielsch, L. Schultz, K. H. Müller, T. G. Woodcock, and O. Gutfleisch,

- Magnetocaloric properties and specifics of the hysteresis at the first-order metamagnetic transition in Ni-doped FeRh, [Phys. Rev. Mater.](#) **5**, 064412 (2021).
- [61] Q. Y. Ren, W. D. Hutchison, J. L. Wang, A. J. Studer, and S. J. Campbell, Magnetic and structural transitions tuned through valence electron concentration in magnetocaloric Mn(Co_{1-x}Ni_x)Ge, [Chem. Mater.](#) **30**, 1324 (2018).
- [62] R. Kütterer, H. R. Hilzinger, and H. Kronmüller, The temperature dependence of the coercive field of Co₅Sm magnets, [J. Magn. Magn. Mater.](#) **4**, 1 (1977).